# Efficiency Improvement of Dual-Receiver WPT Systems Based on Partial Power Processing Control

Shunpan Liu, *Student Member, IEEE*, Xing Zhao, *Member, IEEE*, Yihao Wu, *Student Member, IEEE*,
Lingyun Zhou, *Student Member, IEEE*, Yong Li, *Senior Member, IEEE*, Ruikun Mai, *Senior Member, IEEE*,
and Zhengyou He, *Senior Member, IEEE*

***Abstract*—In wireless power transfer (WPT) system for light electric vehicles (LEVs), adopting dual receivers on the receiver side is an available way to offer a high-current power supply. In this article, the partial power processing (PPP) control method is proposed for optimizing the power loss of the dual-receiver WPT system. With the PPP control method, only one of the active rectifiers will be regulated by the variable angle phase-shift (VAPS) modulation to adjust the required power under different load power demands and misalignment situations. As a result, the switching loss of the two active rectifiers, which accounts for a considerable part of the overall power loss with a high operating frequency, can be dramatically reduced. At last, 24 V-50 A-1200 W LEV wireless charging experimental setup to verify the effectiveness of the proposed PPP control method. Compared with the conventional power distribution method based on impedance matching with VAPS, the proposed PPP control method can increase the efficiency by 6%–7% with misalignment situations, achieving the overall efficiency as high as >92% at the heavy load.**

***Index Terms*—Dual receivers, light electric vehicles (LEVs), partial power processing (PPP), power distribution method, wireless power transfer (WPT).**

## I. INTRODUCTION

ALONG with the rapid development of automation industrial production and logistics transportation, light electric vehicles (LEVs) are rapidly spreading worldwide, such as automated guided vehicles, industrial robots, and unmanned vehicles. The traditional fixed-cable-charging system has become an obstacle to improving the automation level of LEVs and further increasing the work efficiency of production and logistics management. Nowadays, wireless power transfer (WPT) technology has become popular and has been widely applied in various applications, e.g., consumer electronics [1]–[4], LEDs [5], [6], and electric vehicles [7]–[13]. Due to its merits, including safety, convenience, and reliability, the WPT system can serve as a flexible and automated power supply solution for LEVs [14]–[20].

While using WPT technology to charge LEVs, several key features need to be considered: 1) to satisfy the voltage class and shorten the charging time, the low-voltage and high-current power supply system is required [15], [19], which is typically 24/36/48 V and more than 50 A; 2) LEVs are so compact that the installation space of which is small, hence the coil size of the WPT system is limited [14], [17]; and 3) the heat dispersion of the receiver side in such a compact space is a severe issue with the required high charging current and high operating frequency [15], [18], [19].

For the low-voltage and high-current output WPT system, reducing the power loss caused by the equivalent series resistances (ESRs) of the receiver coil, which always suffers from the high current stress, is the first challenge. To release the current stress in the receiver coil, the dual-receiver topology, including the dual-receiver coils and the dual rectifiers, is applied in [21] and [22]. Meanwhile, with two paralleled rectifiers, the requirements on the conducting resistance of power MOSFETs can be halved. Additionally, the *LCC–LCC* compensation network can offer not only a constant current in the transmitter coil and a load-independent input current of the rectifier but also another freedom degree to release the current stress and the ampacity requirement in the receiver coil, which are attractive in the high-current output WPT system [21], [22]. Moreover, this compensation network can also reduce the harmonic currents and the corresponding power loss, especially in short air gap applications [19], [23].

For the feature of the limited volume, the receiver coil size of the WPT system should be small, which leads to a small mutual inductance and weakens the system power transfer capacity. To solve these issues, increasing the system operating frequency is a general method to enhance the system power density, which is consensual in power electronic transformers [24], [25].

Manuscript received April 27, 2021; revised August 23, 2021 and November 12, 2021; accepted December 14, 2021. Date of publication December 28, 2021; date of current version February 18, 2022. This work was supported in part by the funding of the National Natural Science Foundation of China under Grant 51907169, in part by the Sichuan Science and Technology Program under Grant 2020YFH0031, in part by Young Elite Scientist Sponsorship Program by CAST, in part by the Star of Science and Technology in Southwest Jiaotong University under Grant 2682021CG018, and in part by the Original Scientific Equipment Cultivation Project in Southwest Jiaotong University under Grant XJ2021KJZK043. Recommended for publication by Associate Editor C. K. Lee. *(Corresponding author: Yong Li.)*

Shunpan Liu, Lingyun Zhou, Yong Li, Ruikun Mai, and Zhengyou He are with the Key Laboratory of Magnetic Suspension Technology and Maglev Vehicle, Ministry of Education, Southwest Jiaotong University, Chengdu 610031, China, and also with the School of Electrical Engineering, Southwest Jiaotong University, Chengdu 610031, China (e-mail: liusp@my.swjtu.edu.cn; zhouly@my.swjtu.edu.cn; leeo1864@163.com; 82009003@qq.com; hezy@home.swjtu.edu.cn).

Xing Zhao is with the School of Physics, Engineering and Technology, University of York, YO10 5DD York, U.K. (e-mail: xing.zhao@york.ac.uk).

Yihao Wu is with the Department of Engineering, University of Cambridge, CB2 1TN Cambridge, U.K. (e-mail: yw7720@ic.ac.uk).

Color versions of one or more figures in this article are available at https://doi.org/10.1109/TPEL.2021.3138435.

Digital Object Identifier 10.1109/TPEL.2021.3138435

For the heat dispersion issue on the receiver side, the requirement for the power loss on the receiver side is stringent. In a WPT system, the power loss on the receiver side can be divided into the ESRs loss of the receiver coils and the elements in compensation networks, the switching loss, and the conducting loss of rectifiers. Currently, the efficiency optimization method of the dual-receiver WPT system is in short supply. In a dual-transmitter WPT system, which is a symmetric topology and has two transmitter coils and two inverters, a classical but conventional method based on impedance matching for improving the overall efficiency is proposed in [26] and [27]. With this method, the equivalent load impedance of each transmitter is regulated to be equal. Thus, the coil loss and the conducting loss can be optimized, and the overall efficiency is improved even under misalignment conditions. Similar ideas and methods have been widely recognized in some WPT systems with multireceivers or multiloads [28], [29], which can also be utilized in the dual-receiver WPT system.

However, the vast switching loss on the rectifiers still lacks sufficient research attention in these methods above. In the low-voltage and high-current output WPT systems, the active rectifier and MOSFETs with ultra-low conducting resistance are always expected to reduce the rectifier conducting loss. However, these kinds of MOSFETs, generally low-voltage Si MOSFETs, always suffer from the slow switching speed and lead to significant switching loss in the rectifier, especially with a high operating frequency. Though the ESRs loss of the receiver coils can be well-limited by adopting the dual-receiver topology and designing the parameters of the *LCC–LCC* compensation network, the switching loss of the rectifiers cannot be easily optimized. In some situations, the switching loss even occupies a significant proportion of the overall power loss.

In general, the optimization of switching loss is still an urgent problem for the compact WPT system. With the rapid development of power electronic materials, some novel SiC [30], [31] and GaN [32]–[34] switching devices are adopted in the WPT systems for improving the switching performance. However, replacing all the switching elements with these novel devices will increase the system cost dramatically. On the other hand, some modulation and control methods are proposed for achieving zero voltage switching (ZVS) operations. In [35], an auxiliary variable inductor is proposed to extend the ZVS operation range on the inverter. In [36] and [37], to achieve ZVS operation on both the inverter and the active rectifier with a wide range, the variable angle phase-shift (VAPS) modulation method is proposed. However, these methods above are always designed to eliminate the turn-ON loss of the MOSFETs and ignore the turn-OFF loss. In fact, the turn-OFF loss is nonnegligible and also occupies a large percentage of the overall power loss [38].

Recently, for the dual-channel power converters, a kind concept of partial power processing (PPP) has been proposed [39]–[42]. The power transfer channels are divided into the main channel and the auxiliary channel. Generally, only a small part of power flows through the auxiliary channel is processed to adjust the load power demands. The main channel operates with nearly no power processing and minimal switching loss. Thus, the total switching loss, even the turn-OFF loss, can be effectively reduced without increasing the control complexity.

In this article, to achieve a high system efficiency and low power loss at the receiver side, the dual-receiver WPT system with the PPP control method is proposed innovatively. The basic idea is to regulate only one rectifier under different output power conditions. Thus, compared with the conventional power distribution method based on impedance matching, the switching loss in the WPT system with the PPP control method can be reduced apparently, especially in light-load conditions.

The contributions of this article are listed as follows.

1) Here, the dual-receiver WPT system for LEVs charging is adopted with the PPP control method for the first time. Within the PPP control, only one active rectifier will be regulated by VAPS modulation to adjust the load current requirement, while the other is fixed at a constant conducting angle with a low switching loss. Thus, the total switching loss on the receiver side can be effectively reduced.
2) Under different charging statuses and coupler misalignments, the PPP control method is strictly formulated, considering the load current requirements and the variation of the mutual inductances. By calculating and comparing the switching loss of the MOSFETs, the operation modes of each active rectifier and its boundary conditions are well designed for further reducing the switching loss on active rectifiers and improving the overall system efficiency.
3) Considering the actual application conditions of the WPT system, a closed-loop control strategy, including the hysteresis control and the PI control, is proposed. The hysteresis control is designed for selecting and switching the operation modes of the receiver with seamless transitions, and the PI control is adopted for regulating the system output power with a well dynamic response. Thus, the power transferred from each receiver coil can be dynamically regulated based on the different load power requirements and the misalignment conditions. According to the closed-loop experiment, the apparent efficiency improvement of the system can be achieved.

## II. ANALYSIS OF THE DUAL-RECEIVER WPT SYSTEM

### A. Circuit Description and Analysis

The proposed WPT system is depicted in Fig. 1. The dual-receiver topology is adopted for increasing the power transfer capacity and alleviating the current stress. $V_{\mathrm{dc}}$ is the dc input voltage, while $V_{\mathrm{out}}$ is the dc output voltage on the load resistance $R_L$. On the transmitter side, a high-frequency inverter ($P_1$–$P_4$) and an LCC compensation network are adopted to offer a constant current in the transmitter coil $L_p$. $L_r$, $C_r$, and $C_p$ are the compensation elements. On the receiver side, two completely similar receivers, i.e., Receiver #1 and Receiver #2, are employed with two parallel-connected active rectifiers ($S_1$–$S_4$, $S_5$–$S_8$). $L_{s1}$ and $L_{s2}$ are the two receiver coils. Similarly, $L_{t1}$, $L_{t2}$, $C_{s1}$, $C_{t1}$, $C_{s2}$, and $C_{t2}$ form the *LCC* compensation networks. By designing $L_{t1}$ and $L_{t2}$ in the *LCC* networks on the receiver side, the current stress of receiver coils can be further reduced.

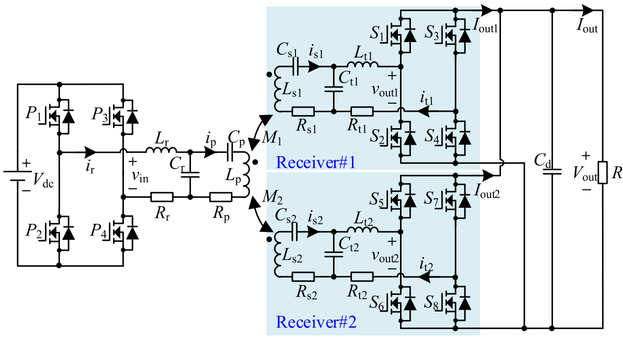

Fig. 1. Schematic diagram of the dual-receiver WPT system with the *LCC–LCC* compensation networks.

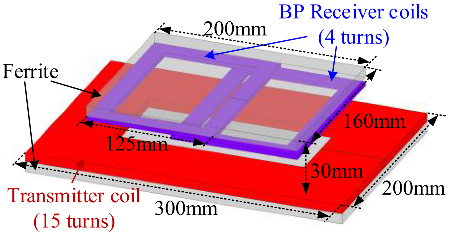

Fig. 2. Model and dimensions of the magnetic coupler.

Moreover, $M_1$ and $M_2$ are the mutual inductances between the transmitter coil and the two receiver coils. $R_r, R_p, R_{s1}, R_{t1}, R_{s2}$, and $R_{t2}$ symbolize the ESRs of each loop.

The magnetic coupler model is designed and shown in Fig. 2. The transmitter coil is square, while the two receiver coils are set as the bipolar (BP) structure to improve misalignment tolerance with nearly no cross-coupling [14]. By designing the receiver coils with the same shape and size, whether the LEV is misaligned on the left or right, one of the receiver coils can be regarded as the main power channel, and the other is the auxiliary power channel. Thus, the system output power can be ensured in different misalignment conditions.

The fundamental harmonic approximation method is used to analyze the WPT system. The equivalent circuit of the proposed WPT system is depicted in Fig. 3. $v_{\text{in}(1)}$ is the fundamental component of the output voltage of the inverter with the operating frequency $f$, while $v_{\text{out1}(1)}$ and $v_{\text{out2}(1)}$ are the fundamental components of the input voltage of the active rectifiers. $Z_{\text{eq1}}$ and $Z_{\text{eq2}}$ are the equivalent load impedances of the two active rectifiers. $Z_f$ is the equivalent reflected impedance at the output side of the inverter.

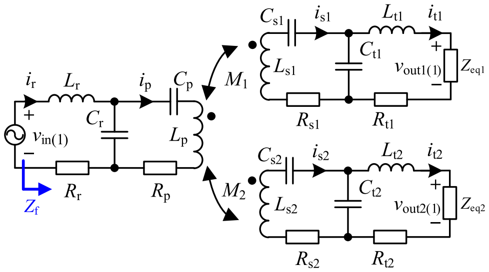

Fig. 3. Equivalent circuit of the proposed WPT system.

To ensure the resonance of each current loop, the compensated capacitors can be obtained as

$$\begin{cases} C_{\text{r}} = (\omega^2 L_{\text{r}})^{-1} & C_{\text{p}} = \left(\omega^2 (L_{\text{p}} - L_{\text{r}})\right)^{-1} \\ C_{\text{t1}} = (\omega^2 L_{\text{t1}})^{-1} & C_{\text{s1}} = \left(\omega^2 (L_{\text{s1}} - L_{\text{t1}})\right)^{-1} \\ C_{\text{t2}} = (\omega^2 L_{\text{t2}})^{-1} & C_{\text{s2}} = \left(\omega^2 (L_{\text{s2}} - L_{\text{t2}})\right)^{-1} \end{cases} \tag{1}$$

where $\omega = 2\pi f$ is the operating angular frequency. Based on Kirchhoff's Voltage Law, while ignoring the ESRs in the circuit, the system can be derived as where

$$\begin{cases} \dot{V}_{\text{out1}(1)} = \dot{I}_{\text{t1}} \cdot Z_{\text{eq1}} \\ \dot{V}_{\text{out2}(1)} = \dot{I}_{\text{t2}} \cdot Z_{\text{eq2}}. \end{cases} \tag{3}$$

Substituting (1) and (3) into (2), the currents in each loop can be obtained as (2) shown as the bottom of this page.

$$\begin{cases} \dot{I}_{\text{r}} = \dot{V}_{\text{in}(1)} \cdot \left( \frac{M_1^2 Z_{\text{eq1}}}{\omega^2 L_{\text{r}}^2 L_{\text{t1}}^2} + \frac{M_2^2 Z_{\text{eq2}}}{\omega^2 L_{\text{r}}^2 L_{\text{t2}}^2} \right) & \dot{I}_{\text{p}} = \frac{\dot{V}_{\text{in}(1)}}{j\omega L_{\text{r}}} \\ \dot{I}_{\text{s1}} = \dot{V}_{\text{in}(1)} \cdot \frac{M_1 Z_{\text{eq1}}}{\omega^2 L_{\text{r}} L_{\text{t1}}^2} & \dot{I}_{\text{t1}} = -\dot{V}_{\text{in}(1)} \cdot \frac{M_1}{j\omega L_{\text{r}} L_{\text{t1}}} \\ \dot{I}_{\text{s2}} = \dot{V}_{\text{in}(1)} \cdot \frac{M_2 Z_{\text{eq2}}}{\omega^2 L_{\text{r}} L_{\text{t2}}^2} & \dot{I}_{\text{t2}} = -\dot{V}_{\text{in}(1)} \cdot \frac{M_2}{j\omega L_{\text{r}} L_{\text{t2}}}. \end{cases} \tag{4}$$

Thus, the currents to voltage gain can be given as follows:

$$\begin{cases} G_{\text{IV1}} = \frac{I_{t1}}{V_{\text{in}(1)}} = \frac{M_1}{\omega L_r L_{t1}} \\ G_{\text{IV2}} = \frac{I_{t2}}{V_{\text{in}(1)}} = \frac{M_2}{\omega L_r L_{t2}} \end{cases} \tag{5}$$

where $I_{t1}$ and $I_{t2}$ are the root-mean-square (rms) values of the input currents of the two active rectifiers, and $V_{\text{in}(1)}$ is the rms value of $v_{\text{in}(1)}$.

According to (5), since $G_{\text{IV1}}$ and $G_{\text{IV2}}$ are not related to the load impedance, the adopted *LCC–LCC* compensation network is therefore ideal to realize the load-independent constant current

$$\begin{cases} \dot{V}_{\text{in}(1)} = \left(j\omega L_{\text{r}} + {}^{1}\!/_{j\omega C_{\text{r}}}\right) \dot{I}_{\text{r}} - {}^{1}\!/_{j\omega C_{\text{r}}} \cdot \dot{I}_{\text{p}} \\ 0 = j\omega M_1 \dot{I}_{\text{s1}} + j\omega M_2 \dot{I}_{\text{s2}} + {}^{1}\!/_{j\omega C_{\text{r}}} \cdot \dot{I}_{\text{r}} + \left(j\omega L_{\text{p}} + {}^{1}\!/_{j\omega C_{\text{r}}} + {}^{1}\!/_{j\omega C_{\text{p}}}\right) \dot{I}_{\text{p}} \\ 0 = j\omega M_1 \dot{I}_{\text{p}} + \left(j\omega L_{\text{s1}} + {}^{1}\!/_{j\omega C_{\text{s1}}} + {}^{1}\!/_{j\omega C_{\text{t1}}}\right) \dot{I}_{\text{s1}} - {}^{1}\!/_{j\omega C_{\text{t1}}} \cdot \dot{I}_{\text{t1}} \\ 0 = j\omega M_2 \dot{I}_{\text{p}} + \left(j\omega L_{\text{s2}} + {}^{1}\!/_{j\omega C_{\text{s2}}} + {}^{1}\!/_{j\omega C_{\text{t2}}}\right) \dot{I}_{\text{s2}} - {}^{1}\!/_{j\omega C_{\text{t2}}} \cdot \dot{I}_{\text{t2}} \\ \dot{V}_{\text{out1}(1)} = \left(j\omega L_{\text{t1}} + {}^{1}\!/_{j\omega C_{\text{t1}}}\right) \dot{I}_{\text{t1}} - {}^{1}\!/_{j\omega C_{\text{t1}}} \cdot \dot{I}_{\text{s1}} \\ \dot{V}_{\text{out2}(1)} = \left(j\omega L_{\text{t2}} + {}^{1}\!/_{j\omega C_{\text{t2}}}\right) \dot{I}_{\text{t2}} - {}^{1}\!/_{j\omega C_{\text{t2}}} \cdot \dot{I}_{\text{s2}} \end{cases} \tag{2}$$

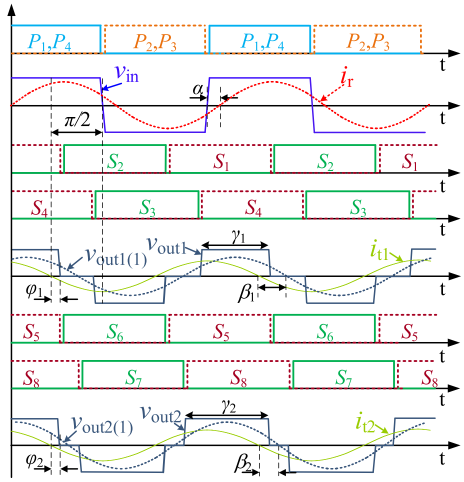

Fig. 4. Waveforms of VAPS control of the WPT system.

output characteristic. Meanwhile, due to the characteristic of the *LCC–LCC* compensation network, the transfer power in each receiver is independent of the other, and no circulation phenomenon will occur while the mutual inductances $M_1$ and $M_2$ are unbalanced. Thus, the system overall efficiency can be ensured with limited complexity of the controller, and the load current $I_{\text{out}}$ is the sum of the output current of the two rectifiers, which should be defined as

$$I_{\text{out}} = I_{\text{out1}} + I_{\text{out2}}. \tag{6}$$

Meanwhile, the load current $I_{\text{out}}$ is also determined by the modulation method and depth of these two active rectifiers.

The load voltage $V_{\text{out}}$ and load power $P_{\text{out}}$ can be derived as

$$V_{\text{out}} = (I_{\text{out1}} + I_{\text{out2}}) \cdot R_L \tag{7}$$

$$P_{\text{out}} = (I_{\text{out1}} + I_{\text{out2}})^2 \cdot R_L. \tag{8}$$

In addition, according to (4), the equivalent impedance $Z_f$ reflected on the transmitter side can be solved as

$$Z_f = \frac{\dot{V}_{\text{in}(1)}}{\dot{I}_r} = \frac{\omega^2 L_r^2}{\left(\frac{M_1^2}{L_{t1}^2} Z_{\text{eq1}} + \frac{M_2^2}{L_{t2}^2} Z_{\text{eq2}}\right)}. \tag{9}$$

### B. VAPS Modulation Method

The VAPS modulation method is adopted in this article to regulate the output power of the active rectifiers while realizing the ZVS operation of the converters. With different load power requirements, the conducting angles of the rectifiers should be dynamically adjusted. To offer enough power supply for the load requirement, the duty cycles of the active rectifiers should be 50%. However, when the required load power is reduced caused by the variations of the battery charging conditions, the conducting angles of active rectifiers should be reduced accordingly.

Fig. 4 shows the key waveforms of the converters. The inverter operates at a constant frequency, a fixed duty cycle, and a zero phase-shift angle. Thus, the fundamental component of the output voltage of the inverter can be expressed as

$$V_{\text{in}(1)} = 2\sqrt{2}V_{\text{dc}} \Big/ \pi. \tag{10}$$

Meanwhile, as shown in Fig. 4, while using VAPS modulation in the active rectifier, adjusting the conducting angle of the active rectifier $\gamma_1$ ($\gamma_2$) and the phase difference between the input current and voltage of the rectifier $\beta_1$ ($\beta_2$) is available to regulate the system output power. $\varphi_1$ ($\varphi_2$) is the phase difference between the positive-to-negative zero-crossing point of $i_{t1}$ ($i_{t2}$) and $S_1$ ($S_5$), which is always expected to be a tiny positive value to ensure the ZVS operation of all MOSFETs in rectifiers. $\gamma_1$ ($\gamma_2$) and $\beta_1$ ($\beta_2$) should satisfy

$$\begin{cases} \beta_1 = \varphi_1 + \frac{\pi-\gamma_1}{2} > \frac{\pi-\gamma_1}{2} \\ \beta_2 = \varphi_2 + \frac{\pi-\gamma_2}{2} > \frac{\pi-\gamma_2}{2}. \end{cases} \tag{11}$$

For the sake of analysis, Receiver #1 is picked up for analyzing the circuit model of the receiver side as an example since the operation principles of both receivers are the same.

Here, the output voltage and current of the rectifier can be expressed as

$$V_{\text{out1}(1)} = \frac{2\sqrt{2}}{\pi} V_{\text{out}} sin\left(\frac{\gamma_1}{2}\right) \tag{12}$$

$$I_{\text{out1}} = \frac{2\sqrt{2}}{\pi} \cdot \left(\sin\left(\frac{\gamma_1}{2}\right) \cdot \cos\left(\frac{\pi-\gamma_1}{2} + \varphi_1\right)\right) \cdot I_{t1}. \tag{13}$$

According to (13), the conducting angle $\gamma_1$ can be derived as

$$\gamma_1 = \varphi_1 + \arccos\left(\cos(\varphi_1) - \frac{\sqrt{2}\pi I_{\text{out1}}}{2 I_{t1}}\right). \tag{14}$$

Substituting (4), (10), and (12) into (3), the equivalent impedance $Z_{\text{eq1}}$ can be derived as

$$Z_{\text{eq1}} = \frac{\dot{V}_{\text{out1}(1)}}{\dot{I}_{t1}} = \frac{\omega L_r L_{t1} V_{\text{out}}}{V_{\text{dc}} M_1} \cdot sin\left(\frac{\gamma_1}{2}\right) \cdot (\cos(\beta_1) + j \cdot \sin(\beta_1)). \tag{15}$$

Then, according to (4) and (15), the rms value of the current in the receiver coil $I_{s1}$ can be derived as

$$I_{s1} = \frac{2\sqrt{2}V_{\text{out}}}{\pi \omega L_{t1}} sin\left(\frac{\gamma_1}{2}\right). \tag{16}$$

Besides, according to the waveforms in Fig. 4, it is evident that only $S_1$ and $S_2$ can turn-OFF at a nearly zero current, and the turn-OFF current of $S_3$ and $S_4$ are still large. Here, the turn-OFF loss of the MOSFET can be regarded to be proportional to the turn-OFF current. Thus, though the ZVS operation can be achieved in the rectifiers with the VAPS modulation method, the turn-OFF losses still take large parts of the overall power loss, especially with the high operating frequency. Table I presents the turn-OFF angles of the MOSFETs in the rectifiers. Since $\varphi_1$ ($\varphi_2$) is a constant tiny positive angle, the turn-OFF loss is mainly determined by the conducting angle $\gamma_1$ ($\gamma_2$).

TABLE I
TURN-OFF ANGLES OF THE MOSFETS IN RECEIVER #1

| | $S_1$ | $S_2$ | $S_3$ | $S_4$ |
|---|---|---|---|---|
| turn-OFF angle | $\varphi_1$ | $\varphi_1$ | $\varphi_1+\pi-\gamma_1$ | $\varphi_1+\pi-\gamma_1$ |

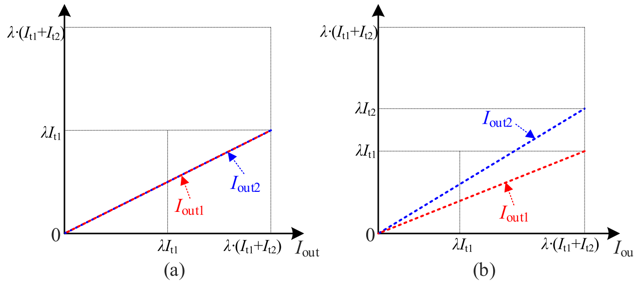

Fig. 5. $I_{\mathrm{out1}}$ and $I_{\mathrm{out2}}$ against $I_{\mathrm{out}}$ with the conventional power distribution method when (a) $M_1 = M_2$ and (b) $M_1 < M_2$.

## C. Conventional Power Distribution Method Based on Impedance Matching

In the whole charging process of vehicle batteries, the variation range of the load resistance is extensive. In the dual-receiver WPT system, for the same $P_{\mathrm{out}}$, there will be many different power distribution schemes between the two receivers. Here, to reduce the power loss on the receiver side, including the ESRs loss and the rectifier loss, the optimal power distribution scheme should be figured out.

In the WPT systems with multitransmitters (receivers), the power distribution method based on impedance matching is already proposed [26]–[29]. Whether the mutual inductances between the transmitter coils and receiver coils are equal or not, the balance of current in each coil is always expected. The output current distribution with the conventional power distribution method is given in Fig. 5.

For the sake of analysis, it is assumed that $M_1 \leq M_2$. Besides, to achieve the ZVS operation in both rectifiers, here $\varphi_1$ and $\varphi_2$ are set as a constant value $\varphi$ and $\lambda = \frac{2\sqrt{2}}{\pi}\cos(\varphi)$ is defined.

*1) $M_1 = M_2$ With the Conventional Power Distribution Method:* As shown in Fig. 5(a), when $M_1 = M_2$, the rectifiers are regulated to output the same current, i.e., $I_{\mathrm{out1}} = I_{\mathrm{out2}}$ and $\gamma_1 = \gamma_2$. According to (6) and (13), the system output current meets

$$\begin{aligned} I_{\mathrm{out}} &= \frac{4\sqrt{2}}{\pi}\cdot\left(\sin\left(\frac{\gamma_1}{2}\right)\cdot\cos\left(\frac{\pi-\gamma_1}{2}+\varphi\right)\right)\cdot I_{t1} \\ &= \frac{4\sqrt{2}}{\pi}\cdot\left(\sin\left(\frac{\gamma_2}{2}\right)\cdot\cos\left(\frac{\pi-\gamma_2}{2}+\varphi\right)\right)\cdot I_{t2}. \end{aligned} \tag{17}$$

Thus, the switching losses of the rectifiers are totally the same.

*2) $M_1 < M_2$ With the Conventional Power Distribution Method:* To release the ESRs losses and the current stresses of the receiver coils, with the conventional power distribution method, $I_{s1}$ and $I_{s2}$ are always regulated as the same value. According to (16), when $M_1 < M_2$, to ensure the balance between $I_{s1}$ and $I_{s2}$, $\gamma_1 = \gamma_2$ is also necessary since $L_{t1} = L_{t2}$. Thus, as shown in Fig. 5(b), the ratio of $I_{\mathrm{out1}}$ and $I_{\mathrm{out2}}$ is the same as the ratio of $I_{t1}$ and $I_{t2}$. The system output current meets

$$\begin{aligned} I_{\mathrm{out}} &= \frac{2\sqrt{2}}{\pi}\cdot\left(\sin\left(\frac{\gamma_1}{2}\right)\cdot\cos\left(\frac{\pi-\gamma_1}{2}+\varphi\right)\right)\cdot(I_{t1}+I_{t2}) \\ &= \frac{2\sqrt{2}}{\pi}\cdot\left(\sin\left(\frac{\gamma_2}{2}\right)\cdot\cos\left(\frac{\pi-\gamma_2}{2}+\varphi\right)\right)\cdot(I_{t1}+I_{t2}). \end{aligned} \tag{18}$$

Moreover, according to (9) and (15), the reflected impedance $Z_f$ can be derived as

$$Z_f = \frac{\omega L_r V_{\mathrm{dc}}}{\begin{pmatrix} \frac{M_1}{L_{t1}}\cdot \mathit{sin}\left(\frac{\gamma_1}{2}\right)\cdot(\cos(\beta_1)+j\cdot\sin(\beta_1)) \\ +\frac{M_2}{L_{t2}}\cdot \mathit{sin}\left(\frac{\gamma_2}{2}\right)\cdot(\cos(\beta_2)+j\cdot\sin(\beta_2)) \end{pmatrix}\cdot V_{\mathrm{out}}}. \tag{19}$$

## D. Power Loss Calculation

To clarify the main factors affecting the overall power loss, the power loss model is established and analyzed as follows.

*1) ESRs Loss:* The ESRs loss consists of the power loss on the coils, inductors, and compensated capacitors, which can be derived as

$$\begin{aligned} P_{\mathrm{ESRs}} &= P_{\mathrm{ESRs\_rec}} + P_{\mathrm{ESRs\_tran}} \\ &= I_{s1}^2 R_{s1} + I_{s2}^2 R_{s2} + I_{t1}^2 R_{t1} + I_{t2}^2 R_{t2} + I_r^2 R_r + I_p^2 R_p \end{aligned} \tag{20}$$

where $P_{\mathrm{ESRs\_rec}}$ and $P_{\mathrm{ESRs\_tran}}$ indicate the ESRs losses on the receiver side and the transmitter side, respectively.

*2) Active Rectifiers Loss:* The power loss on the active rectifiers $P_{\mathrm{rec}}$ can be divided into the conducting loss and the switching loss, i.e.,

$$P_{\mathrm{rec}} = P_{\mathrm{rec\_cond}} + P_{\mathrm{rec\_sw}} \tag{21}$$

where $P_{\mathrm{rec\_cond}}$ presents the conducting loss of the MOSFETs in rectifiers and $P_{\mathrm{rec\_sw}}$ presents its switching loss. Ignoring the conducting loss on the anti-paralleled diodes of the MOSFETs, which occupies a tiny part of $P_{\mathrm{rec}}$, $P_{\mathrm{rec\_cond}}$ can be expressed as

$$P_{\mathrm{rec\_cond}} = 2\cdot\left(I_{t1}^2 + I_{t2}^2\right)\cdot R_{\mathrm{rec\_sd}} \tag{22}$$

where $P_{\mathrm{rec\_sd}}$ is the conducting resistance of the MOSFETs in the rectifier, which can be found or fitted from the datasheet of the MOSFET. Meanwhile, with the VAPS modulation method, $P_{\mathrm{rec\_sw}}$ can be expressed as [43], [44]

$$\begin{aligned} P_{\mathrm{rec\_sw}} &= 2\sqrt{2}\left(A_{\mathrm{rec}} + B_{\mathrm{rec}}\right)V_{\mathrm{out}}f \\ &\quad\cdot\begin{pmatrix} I_{t1}\cdot(|\sin(\varphi_1)| + |\sin(\varphi_1+\pi-\gamma_1)|) \\ +I_{t2}\cdot(|\sin(\varphi_2)| + |\sin(\varphi_2+\pi-\gamma_2)|) \end{pmatrix} \end{aligned} \tag{23}$$

where $A_{\mathrm{rec}} = E_{\mathrm{rec\_off}}/(U_{\mathrm{rec\_DD}} I_{\mathrm{rec\_D}})$ indicates the value of the turn-OFF energy of the MOSFETs in the rectifier at the standard test condition, and $B_{\mathrm{rec}} = Q_{\mathrm{rec\_DD}}/I_{\mathrm{rec\_RD}}$ indicates the value of the switching loss of the anti-paralleled diodes. $E_{\mathrm{rec\_off}}$, $U_{\mathrm{rec\_DD}}$, $I_{\mathrm{rec\_D}}$, $Q_{\mathrm{rec\_DD}}$, and $I_{\mathrm{rec\_RD}}$ can be found in the datasheet

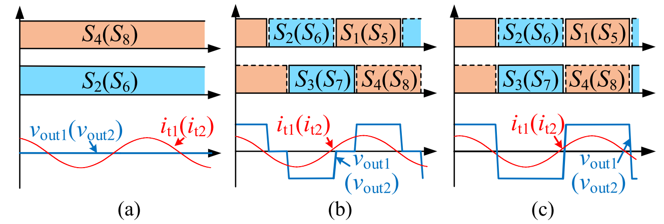

Fig. 6. Waveforms of the rectifiers with (a) shutting status, (b) VAPS modulation, and (c) full-load status.

TABLE II
OPERATION MODES OF THE RECTIFIERS IN FOUR MODES

| Operation mode | The status of Rec#1 | The status of Rec#2 |
|---|---|---|
| Mode 1 | VAPS | Shutting |
| Mode 2 | Shutting | VAPS |
| Mode 3 | Full-load | VAPS |
| Mode 4 | VAPS | Full-load |

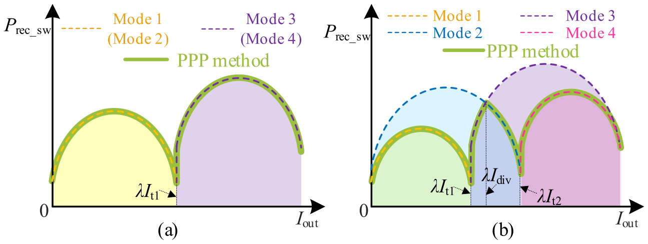

Fig. 7. Total switching loss on the active rectifiers $P_{\text{rec\_sw}}$ against $I_{\text{out}}$ when (a) $M_1 = M_2$ and (b) $M_1 < M_2$.

or tested/modeled by the users. The modeling and calculating methods have already been introduced in [38] and [45]. Although the calculated switching loss cannot be completely accurate, the results still have a substantial reference value.

*3) Inverter Loss:* The inverter loss can also be expressed as

$$P_{\text{inv}} = P_{\text{inv\_cond}} + P_{\text{inv\_sw}} \tag{24}$$

where the conducting loss $P_{\text{inv\_cond}}$ and the switching loss $P_{\text{inv\_sw}}$ can be expressed as

$$P_{\text{inv\_cond}} = 2 \cdot I_r^2 \cdot R_{\text{inv\_ds}} \tag{25}$$

$$P_{\text{inv\_sw}} = 4\sqrt{2}\left(A_{\text{inv}} + B_{\text{inv}}\right) V_{\text{dc}} I_r f \left|\sin\left(\alpha\right)\right| \tag{26}$$

where $A_{\text{inv}} = E_{\text{inc\_off}}/(E_{\text{U\_DD}} I_{\text{inv\_D}})$ and $B_{\text{inv}} = Q_{\text{inv\_DD}}/I_{\text{inv\_RD}}$ indicate the corresponding turn-OFF loss in the inverter. Similarly, $R_{\text{inv\_ds}}$, $E_{\text{inv\_off}}$, $U_{\text{inv\_DD}}$, $I_{\text{inv\_D}}$, $Q_{\text{inv\_DD}}$, and $I_{\text{inv\_RD}}$ can be found in the datasheet or tested/modeled by the users. Here, $\alpha$ is the phase difference between $v_{\text{in}(1)}$ and $i_r$, which can be defined as

$$\alpha = \arctan\left(\frac{\text{Im}\left(Z_f\right)}{\text{Re}\left(Z_f\right)}\right). \tag{27}$$

## III. PROPOSED PPP-BASED POWER DISTRIBUTION METHOD

With the conventional power distribution scheme, the receiver coil losses can be reduced. However, while utilizing the low-conducting-resistance MOSFETs to release the conducting loss of the rectifier with such high output current, their poor switching performance should also be well considered. While regulating the system output power by adjusting the conducting angle of the rectifiers, the switching losses of the rectifiers account for the majority of the total power loss on the receiver side even the ZVS operation is achieved.

### A. Principle of the PPP Control With VAPS Modulation

With the adoption of VAPS modulation, there are three statuses for the active rectifiers, and the waveforms of each status are given in Fig. 6. With the shutting status in Fig. 6(a), only the low-side MOSFETs, i.e., $S_2$ $(S_6)$ and $S_4$ $(S_8)$, are continuously conducting. Thus, $v_{\text{out1}}$ $(v_{\text{out2}})$ and the output power of the rectifier are zero. In this situation, the switching loss of the rectifier can be ignored since there is no switching operation. While the rectifier is regulated by VAPS modulation and $\gamma_1$ $(\gamma_2)$ is less than $\pi$, as shown in Fig. 6(b), $I_{\text{out1}}$ $(I_{\text{out2}})$ is determined by $\gamma_1$ $(\gamma_2)$. Meanwhile, according to (23), the turn-OFF loss of the rectifier should be taken into account even the ZVS operation is achieved. While $\gamma_1$ $(\gamma_2)$ reaches $\pi$, which is the full-load status in Fig. 6(c), the rectifier will operate with its maximum output current. Then, the switching loss of the rectifier is limited since the turn-OFF currents are nearly zero when MOSFETs turn-OFF.

Obviously to decrease the switching losses of the rectifiers, adjusting the output current of only one rectifier while keeping the other in shutting or full-load status is a workable way. Based on this idea, the PPP control method for the WPT system is proposed in this article. According to the load power requirements, the operation modes of the receiver can be divided into the following four modes, as shown in Table II.

Here, only one rectifier will be modulated by the VAPS method to adjust the output power dynamically. The other rectifier will operate at the full-load status with a low turn-OFF current or shut down with no switching operating. Since the switching loss of a single MOSFET can be regarded to be proportional to its turn-OFF current, the switching loss on the rectifier with full-load or shutting mode can be well limited. Besides, with the unbalanced $M_1$ and $M_2$, the PPP method must be adjusted to suit different misalignment conditions.

According to the analysis of the turn-OFF current and the receiver operation mode, the trends of total switching loss on the active rectifiers $P_{\text{rec\_sw}}$ with different operation modes against the output current $I_{\text{out}}$ are plotted in Fig. 7. When $M_1 = M_2$, the results of the two groups (Mode 1 = Mode 2 and Mode 3 = Mode 4) are the same. Therefore, the operation of the rectifiers can be divided into two modes with the variation of $I_{\text{out}}$. According to (14) and (23), the trend of $P_{\text{rec\_sw}}$ against $I_{\text{out}}$ is plotted as the solid green curve in Fig. 7(a). Besides, when $M_1 \neq M_2$, the operation of the rectifiers will be divided into four modes. Since there are overlaps between the four operation modes, the one with lower $P_{\text{rec\_sw}}$ should be picked up as the selected operation mode. By combining the curve of the selected modes, the final trend of $P_{\text{rec\_sw}}$ is plotted as the solid green curve in Fig. 7(b).

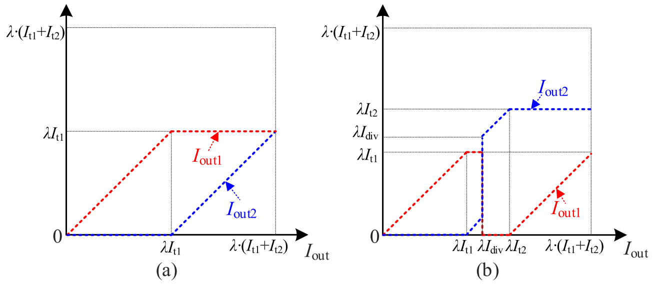

Fig. 8. Output current $I_{\text{out1}}$ and $I_{\text{out2}}$ against $I_{\text{out}}$ with the proposed PPP control method when (a) $M_1 = M_2$ and (b) $M_1 < M_2$.

TABLE III

SYSTEM SPECIFICATION AND PARAMETER VALUES

| *Symb.* | *Val.* | *Symb.* | *Val.* | *Symb.* | *Val.* |
|---|---|---|---|---|---|
| $V_{\text{dc}}$ | 350V | $V_{\text{out}}$ | 24V | $I_{\text{out}}$ | 5~50A |
| $L_{\text{r}}$ | 29.5μH | $C_{\text{r}}$ | 21.46nF | $R_{\text{r}}$ | 40mΩ |
| $L_{\text{p}}$ | 90.4μH | $C_{\text{p}}$ | 10.4nF | $R_{\text{p}}$ | 220.1mΩ |
| $L_{\text{t1}}$ | 2.63μH | $C_{\text{t1}}$ | 240.8nF | $R_{\text{t1}}$ | 2.9mΩ |
| $L_{\text{t2}}$ | 2.64μH | $C_{\text{t2}}$ | 239.9nF | $R_{\text{t2}}$ | 2.9mΩ |
| $L_{\text{s1}}$ | 6.92μH | $C_{\text{s1}}$ | 147.6nF | $R_{\text{s1}}$ | 23.0mΩ |
| $L_{\text{s2}}$ | 7.09μH | $C_{\text{s2}}$ | 142.3nF | $R_{\text{s2}}$ | 24.1mΩ |
| $f$ | 200kHz | $S_1$-$S_8$ | IXFX420N10T | $A_{\text{rec}}$+ $B_{\text{rec}}$ | 138ns |
| Air gap | 30mm | $P_1$-$P_4$ | C3M0021120D | $A_{\text{inv}}$+ $B_{\text{inv}}$ | 34.2ns |

### *B. Power Distribution Scheme of the PPP Control*

Based on the selected operation modes, the distribution scheme of rectifier output currents with the PPP control method is depicted in Fig. 8.

*1)* M*₁* = M₂ *With the PPP Method:* The trends of $I_{\text{out1}}$ and $I_{\text{out2}}$ against $I_{\text{out}}$ with the proposed PPP control method when $M_1 = M_2$ are shown in Fig. 8(a). To release $P_{\text{rec\_sw}}$, when $I_{\text{out}} \leq \lambda I_{t1}$, only $\gamma_1$ is adjusted, and Receiver #2 is shut down with no switching loss, i.e.,

$$\begin{cases} I_{\text{out1}} = I_{\text{out}} = \frac{2\sqrt{2}}{\pi} \cdot \left(\sin\left(\frac{\gamma_1}{2}\right) \cdot \cos\left(\frac{\pi-\gamma_1}{2} + \varphi\right)\right) \cdot I_{t1} \\ I_{\text{out2}} = 0. \end{cases} \tag{28}$$

While $I_{\text{out}} > \lambda I_{t1}$, $\gamma_1$ is fixed at $\pi$, and the rectifier in Receiver #2 is adjusted to suit the rest of the load required current, i.e.,

$$\begin{cases} I_{\text{out1}} = \lambda \cdot I_{t1} \\ I_{\text{out2}} = I_{\text{out}} - I_{\text{out1}} = \frac{2\sqrt{2}}{\pi} \cdot \\ \left(\sin\left(\frac{\gamma_2}{2}\right) \cdot \cos\left(\frac{\pi-\gamma_2}{2} + \varphi\right)\right) \cdot I_{t2}. \end{cases} \tag{29}$$

Thus, in each operating condition, only one rectifier is dynamically adjusted with limited switching loss, while the other rectifier could operate with nearly no switching loss.

*2)* M*₁* < M₂ *With PPP Method:* Moreover, if $M_1$ and $M_2$ are unbalanced, the power distribution method should consider not only the total switching loss on the rectifiers but also the capacity of the output current from the single rectifier. While $M_1 < M_2$, the trends of $I_{\text{out1}}$ and $I_{\text{out2}}$ against $I_{\text{out}}$ are shown in Fig. 8(b). When $I_{\text{out}} \leq \lambda I_{t1}$, similarly, only $\gamma_1$ is adjusted, and Receiver #2 is shut down, i.e., the receiver operates in Mode 1. The output current of each receiver meets (28).

When $\lambda I_{t1} < I_{\text{out}} \leq \lambda I_{t2}$, there are two possible operation modes of the receiver. Because the output current of Receiver #1 cannot ever satisfy the required power, Receiver #2 must be utilized for power transmission individually or cooperatively. To choose the more suitable operation mode, $I_{\text{div}}$ is defined as the boundary line of this load range and can be calculated by comparing the switching losses of Mode 2 and Mode 3.

While $\lambda I_{t1} < I_{\text{out}} \leq \lambda I_{\text{div}}$, by comparing the switching losses of the possible operation modes, $\gamma_1$ should still be fixed at $\pi$, and $\gamma_2$ is adjusted to suit the rest of the load required current, which indicates that the receiver operates in Mode 3. The output current of each receiver meets (29). While $\lambda I_{\text{div}} < I_{\text{out}} \leq \lambda I_{t2}$, only $\gamma_2$ is adjusted, and Receiver #1 is shut down with no switching loss. In this case, the receiver operates in Mode 2, i.e.,

$$\begin{cases} I_{\text{out1}} = 0 \\ I_{\text{out2}} = I_{\text{out}} = \frac{2\sqrt{2}}{\pi} \cdot \left(\sin\left(\frac{\gamma_2}{2}\right) \cdot \cos\left(\frac{\pi-\gamma_2}{2} + \varphi\right)\right) \cdot I_{t2}. \end{cases} \tag{30}$$

Additionally, when $I_{\text{out}} > \lambda I_{t2}$, to ensure the required power, $\gamma_2$ is still fixed at $\pi$, and $\gamma_1$ is adjusted to suit the rest of the load required current. Here, the receiver operates in Mode 4, i.e.,

$$\begin{cases} I_{\text{out1}} = I_{\text{out}} - I_{\text{out2}} = \frac{2\sqrt{2}}{\pi} \cdot \\ \left(\sin\left(\frac{\gamma_1}{2}\right) \cdot \cos\left(\frac{\pi-\gamma_1}{2} + \varphi\right)\right) \cdot I_{t1} \\ I_{\text{out2}} = \lambda \cdot I_{t2}. \end{cases} \tag{31}$$

### *C. Power Loss Analysis and Comparison*

To verify the effect of the proposed PPP control on the efficiency improvement in the dual-receiver WPT system, analysis and comparison of the power loss in each part are necessary. The corresponding mathematical model has been introduced in Section II, and the system parameters are listed in Table III.

According to the system circuit and power loss analysis below, the theoretical power loss comparison is shown in Fig. 9. The rectifier switching loss $P_{\text{rec\_sw}}$ with the conventional power distribution method under different ratios of $M_1$ to $M_2$ and $I_{\text{out}}$ is shown in Fig. 9(a). Here, $P_{\text{rec\_sw}}$ is independent of $M_1/M_2$ and is affected by $I_{\text{out}}$. While the system is controlled by the PPP method, as shown in Fig. 9(b), $P_{\text{rec\_sw}}$ is well limited since only one rectifier is dynamically regulated, and the other rectifier operates with a tiny turn-OFF current or even be shut down. This result is consistent with the theoretical analysis.

Meanwhile, the ESRs loss on the receiver side $P_{\text{ESRs\_rec}}$ and the rectifier conducting loss $P_{\text{rec\_cond}}$ with these two power distribution methods are plotted in Fig. 9(c) and (d). With the low ESRs of the small size receiver coils and the designed compensation parameters, $P_{\text{ESRs\_rec}}$ is well limited. In theory, although the PPP control method will increase $P_{\text{ESRs\_rec}}$, this part of power loss is still a tiny part of the overall system power loss. Meanwhile, by utilizing the IXFX420N10T in the rectifier, the rectifier conducting loss $P_{\text{rec\_cond}}$ is also kept at a low level. What needs to be emphasized is that $P_{\text{ESRs\_rec}}$ and $P_{\text{rec\_cond}}$ of the system adopting these two power distribution methods have nearly no difference. Thus, while $P_{\text{rec\_sw}}$ is reduced, the improvement of the system efficiency is significant.

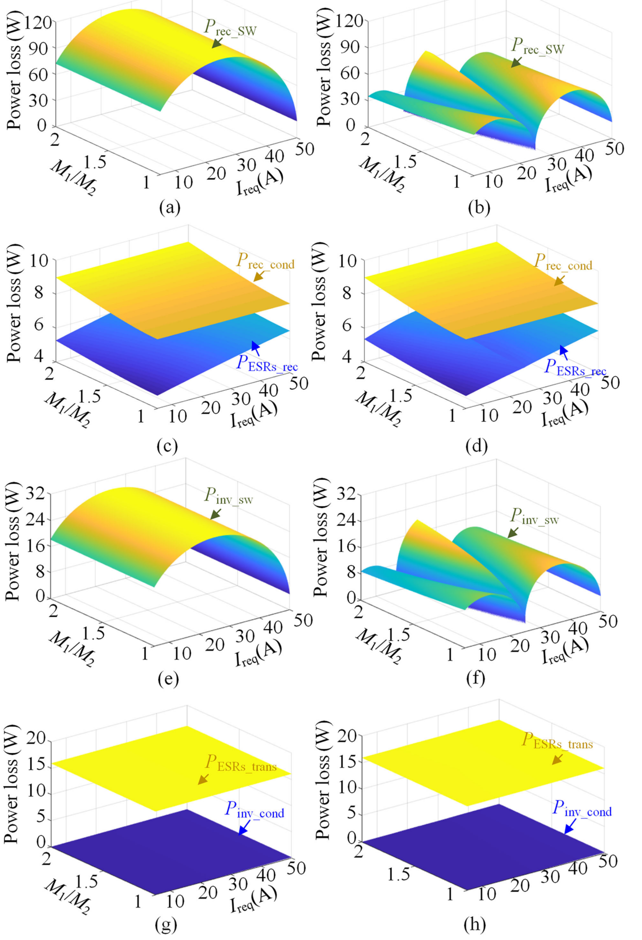

Fig. 9. Calculated power loss of each part: (a) $P_{\text{rec\_sw}}$ with the conventional power distribution method, (b) proposed PPP control method, (c) $P_{\text{rec\_cond}}$ and $P_{\text{ESRs\_rec}}$ with the conventional power distribution method, and (d) proposed PPP control method, (e) $P_{\text{inv\_sw}}$ with the conventional power distribution method, (f) proposed PPP control method, (g) $P_{\text{inv\_cond}}$ and $P_{\text{ESRs\_tran}}$ with the conventional power distribution method, and (h) proposed PPP control method.

The switching losses of the inverter with different power distribution methods are plotted in Fig. 9(e) and (f). The curves of $P_{\text{inv\_sw}}$ have similar trends of $P_{\text{rec\_sw}}$, which indicates the effectiveness of the proposed PPP control for reducing the inverter switching loss. Here, by utilizing C3M0021120D in the inverter, $P_{\text{inv\_sw}}$ accounts for a limited part of the overall system loss. The comparisons of $P_{\text{inv\_cond}}$ and $P_{\text{ESRs\_tran}}$ are shown in Fig. 9(g) and (h). Similarly, $P_{\text{inv\_cond}}$ and $P_{\text{ESRs\_tran}}$ of the system adopting these two power distribution methods have nearly no difference and occupy a small percentage of the overall system power loss.

### *D. Control Strategy and the Diagram of the PPP Control*

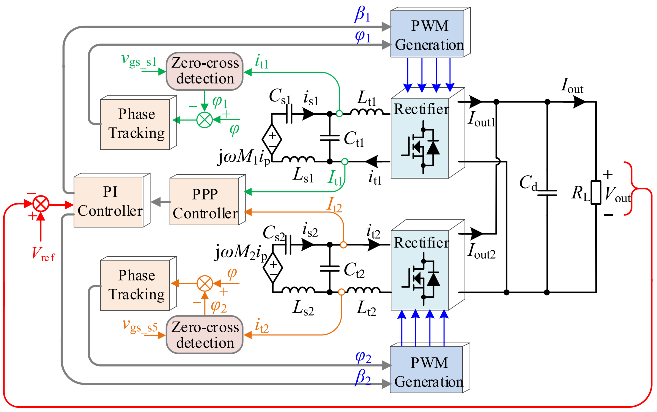

Fig. 10. Control diagram of the PPP-based controller on the receiver side.

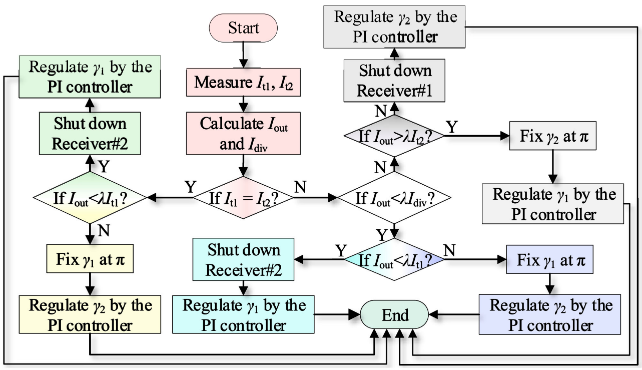

Fig. 11. Flowchart of the PPP-based power distribution strategy.

The control diagram of the receiver side is depicted in Fig. 10. The main control goal is to provide the required power depending on the charging state of the vehicle battery. Meanwhile, the ZVS operation should also be realized reliably. Within these control goals, the flowchart of the proposed PPP control is designed in Fig. 11.

First, while $I_{t1}$ and $I_{t2}$ are measured and input to the PPP controller, the boundary lines of the different operation modes can be obtained. Meanwhile, the system output current $I_{\text{out}}$ can be calculated with the known $\beta_1$ and $\beta_2$. By comparing the $I_{\text{out}}$, $I_{t1}$, $I_{t2}$, and the calculated $I_{\text{div}}$, the receiver operation mode can be selected with hysteresis control in the PPP controller. Only one active rectifier will be dynamically adjusted by the PI controller with the measured $V_{\text{out}}$ and the reference output $V_{\text{ref}}$, while the other is fixed with a constant conducting angle $\pi$ or 0. Second, the phases of $i_{t1}$ and $i_{t2}$ are obtained by using zero-cross detection. With the assistance of the phase comparison circuits, phase differences $\varphi_1$ and $\varphi_2$ are controlled to track the reference angle $\varphi$. Thus, the ZVS operations can be guaranteed. By testing the switching performance of the MOSFETs under the whole power range, $\varphi$ is set as 5° here as an example.

Moreover, to determine and transit the operation modes, considering the characteristics of Mode 1–Mode 4, an available but straightforward hysteresis control method is designed in the PPP controller. As shown in Fig. 12, due to the output current limitation in Mode 1 and Mode 2, when $I_{\text{out}}$ increased to $\lambda I_{t1}$ ($\lambda I_{t2}$), Receiver #1 (Receiver #2) is not able to provide more power. Thus, the receiver should be switched to Mode 3 (Mode 4) at $I_{\text{out}} = \lambda I_{t1}$ ($I_{\text{out}} = \lambda I_{t2}$). However, according to the

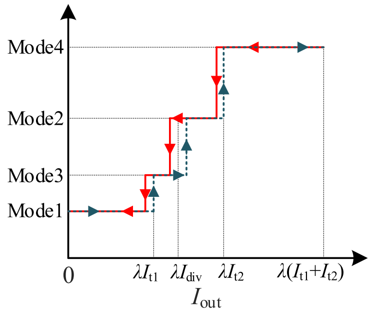

Fig. 12. Diagram of the designed hysteresis control in the PPP controller.

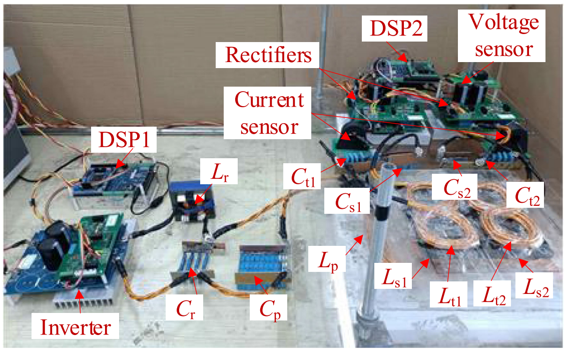

Fig. 13. Schematic diagram of the experimental setup.

experimental test, when the receiver operation mode switches from Mode 3 (Mode 4) to Mode 1 (Mode 2), the hysteresis switching point is set at $I_{\text{out}} = 0.98{\cdot}\lambda I_{t1}$ ($I_{\text{out}} = 0.98{\cdot}\lambda I_{t2}$). Besides, since there is a large overlap in the power coverage of Mode 3 and Mode 2, the switching points between Mode 3 and Mode 2 can be set at $I_{\text{out}} = 1.02\lambda I_{\text{div}}$ and $I_{\text{out}} = 0.98\lambda I_{\text{div}}$.

## IV. EXPERIMENTAL VERIFICATIONS

### A. Experimental Prototype

To verify the validity of the proposed PPP method, a 24 V–50 A–1200-W output experimental prototype is built and shown in Fig. 13, using the parameters in Table III.

Digital signal processors (DSPs) TMS320F28335 are used for dual side controls. The magnetic coupler with the BP receiver coil structure is employed in this experimental prototype. The dimensions of the magnetic coupler are designed with ANSYS MAXWELL software, as shown in Fig. 2. The simulated and experimental mutual inductances $M_1$ and $M_2$ versus $x$-axis misalignment are shown in Fig. 14. Errors of $M_1$ and $M_2$ between the simulation and experiment are subsistent and acceptable, which is caused by the difference between the handmade magnetic coupler and the ideal MAXWELL model. While the magnetic coupler is well-aligned, the coupling coefficient between the single-receiver coil and the transmitter coil is about 0.35. $x{\in}[-60$ mm, 60 mm] is set as the movement range of the receiver coils.

The coils in the experimental setup are shown in Fig. 15. The 20 mm$^2$-Litz-wire is utilized. In Fig. 15(a), the transmitter coil is made by the two-strand paralleled Litz wire. For the BP receiver coils, the single-strand Litz wire is adopted for releasing the weight of the receiver coil since its maximum current is limited in 7 A, as shown in Fig. 15(b). It should be noted that, for further reducing the size and weight of the receiver, refer to the inductor integration methods in [46]–[48], the compensation inductors $L_{t1}$ and $L_{t2}$ are integrated at the outside of the ferrite in the receiver. By designing these inductors in the DD structure, these inductors are well decoupled to the receiver coils and the transmitter coil. Then, the load-independent constant output current is maintained. Meanwhile, since $L_{t1}$ and $L_{t2}$ are only $\sim$2.64 $\mu$H, the cost of the Litz wire is also limited even the inductors are made by the two-strand paralleled Litz wire, as shown in Fig. 15(c).

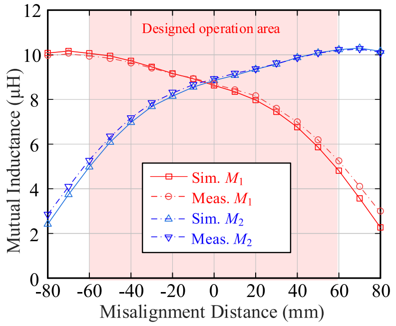

Fig. 14. Simulated and measured $M_1$ and $M_2$ against the misalignment distance.

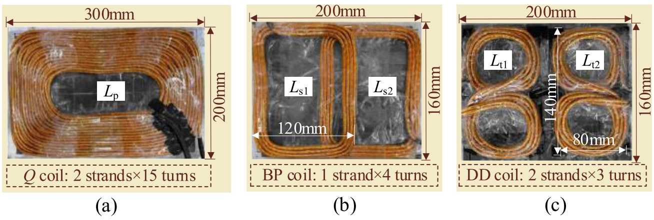

(a) (b) (c)

Fig. 15. Structure and dimensions of (a) transmitter coil, (b) BP receiver coils, and (c) DD comparison inductors.

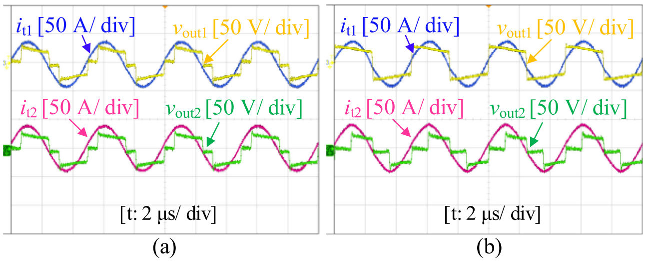

(a) (b)

Fig. 16. Experimental waveforms of $i_{t1}$, $i_{t2}$, $v_{\text{out1}}$, and $v_{\text{out2}}$ with (a) conventional method and (b) PPP control method when $M_1 = M_2$ and $I_{\text{out}} = 37.5$ A.

### B. Experimental Waveforms

*1) Waveforms of* $M_1 = M_2$*:* Fig. 16 shows the waveforms of $i_{t1}$, $i_{t2}$, $v_{\text{out1}}$, and $v_{\text{out2}}$ using two different power distribution

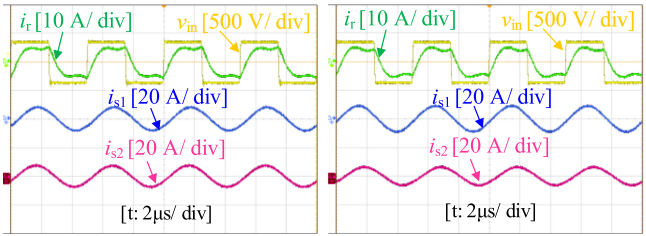

(a) (b)

Fig. 17. Experimental waveforms of $i_r$, $i_{s1}$, $i_{s2}$, and $v_{\text{in}}$ with (a) conventional method and (b) PPP control method when $M_1 = M_2$ and $I_{\text{out}} = 37.5$ A.

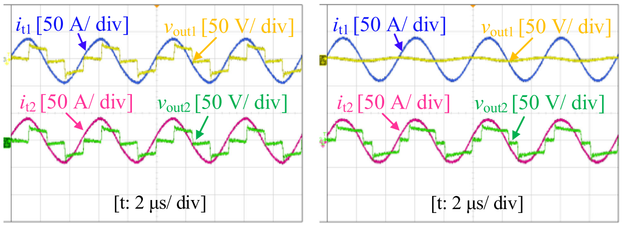

(a) (b)

Fig. 18. Experimental waveforms of $i_{t1}$, $i_{t2}$, $v_{\text{out1}}$, and $v_{\text{out2}}$ with (a) conventional method and (b) PPP method when $M_1 = M_2$ and $I_{\text{out}} = 18.5$ A.

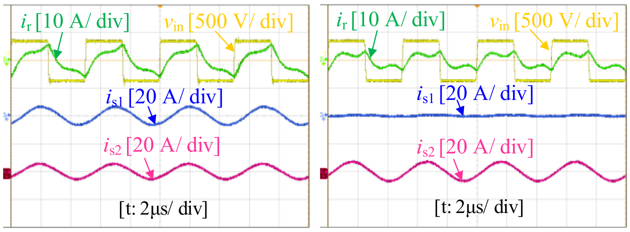

(a) (b)

Fig. 19. Experimental waveforms of $i_r$, $i_{s1}$, $i_{s2}$, and $v_{\text{in}}$ with (a) conventional method and (b) proposed PPP control method when $M_1 = M_2$ and $I_{\text{out}} = 18.5$ A.

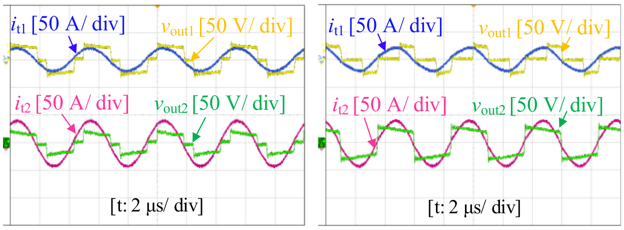

(a) (b)

Fig. 20. Experimental waveforms of $i_{t1}$, $i_{t2}$, $v_{\text{out1}}$, and $v_{\text{out2}}$ with (a) conventional method and (b) PPP control method when $M_1 = 0.5{\cdot}M_2$ and $I_{\text{out}} = 30$ A.

TABLE IV
SYSTEM SPECIFICATION AND PARAMETER VALUES OF THE SINGLE RECEIVER WPT SYSTEM

| *Symb.* | *Val.* | *Symb.* | *Val.* | *Symb.* | *Val.* |
|---|---|---|---|---|---|
| $V_{dc}$ | 350V | $V_{out}$ | 24V | $I_{out}$ | 10~50A |
| $L_{sq}$ | 14.4μH | $C_{sq}$ | 53.8nF | $R_{sq}$ | 60.1mΩ |
| $L_{tq}$ | 2.64μH | $C_{tq}$ | 239.9nF | $R_{tq}$ | 2.5mΩ |
| $f$ | 200kHz | $S_1$-$S_4$ | IXFX420N10T | Air gap | 30mm |

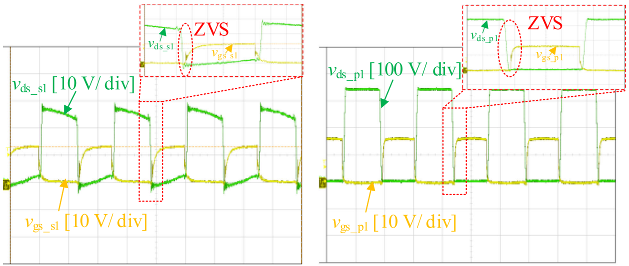

(a) (b)

Fig. 21. Experimental waveforms of (a) $v_{\text{ds\_s1}}$ and $v_{\text{gs\_s1}}$, (b) $v_{\text{ds\_p1}}$ and $v_{\text{gs\_p1}}$ when $M_1 = 0.5{\cdot}M_2$ and $I_{\text{out}} = 30$ A.

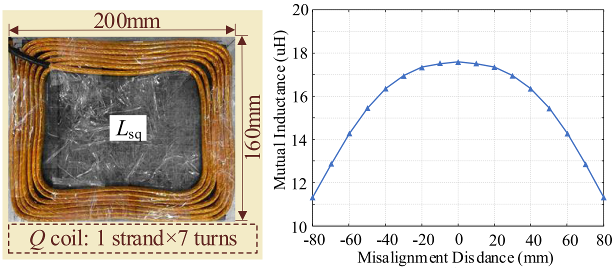

(a) (b)

Fig. 22. (a) Structure and dimensions of the single-receiver coil and (b) mutual inductance $M_q$ against the misalignment distance.

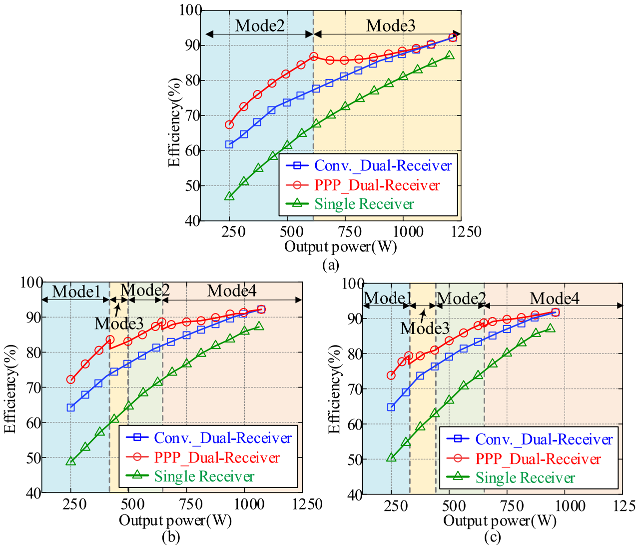

Fig. 23. System efficiency against the output power when the misalignment distance: (a) $x = 0$ mm, (b) $x = -45$ mm, and (c) $x = -60$ mm.

methods in the heavy-load condition ($I_{\text{out}} > \lambda I_{t1}$) with $M_1 = M_2 = 8.7$ $\mu$H. The dc output voltage and current are maintained at 24 V and 37.5 A. In Fig. 16(a), when the conventional power distribution method is applied, rectifiers are regulated to output the same $i_{t1}$ and $i_{t2}$ with the $\gamma_1 = \gamma_2$. Fig. 16(b) shows the corresponding waveforms with the proposed PPP control method. In this case, Receiver #1 is in full-load status with $\gamma_1 = \pi$, and only the rectifier in Receiver #2 is adjusted to suit the load required current.

Fig. 17 compares the waveforms of $i_r$, $i_{s1}$, $i_{s2}$, and $v_{\text{in}}$ using two control methods. When the conventional power distribution

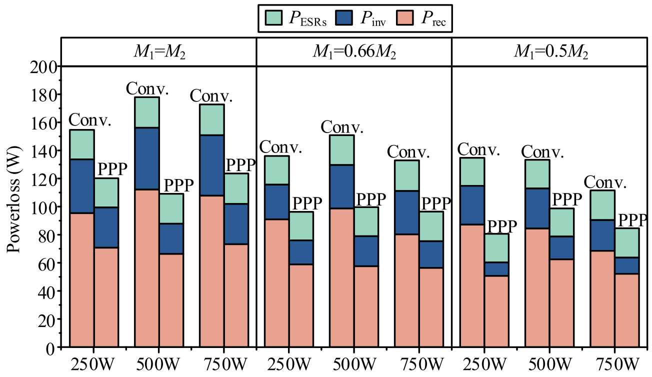

Fig. 24. Experimental power loss distributions with different ratios of $M_1$ to $M_2$.

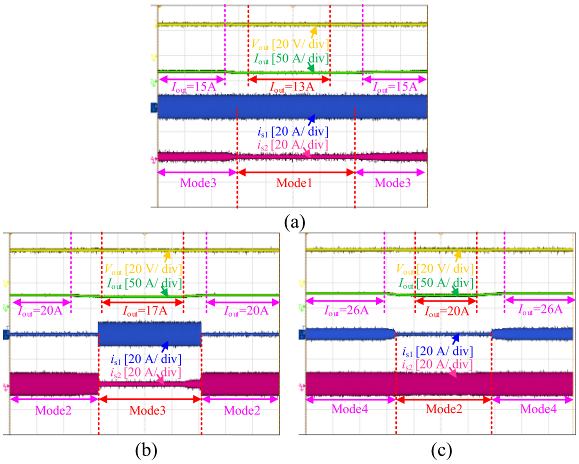

(a)

(b)

(c)

Fig. 25. Experimental dynamic response waveforms of $V_{\text{out}}$, $I_{\text{out}}$, $i_{s1}$, and $i_{s2}$ while (a) switching between Mode 1 and Mode 3, (b) switching between Mode 3 and Mode 2, and (c) switching between Mode 2 and Mode 4.

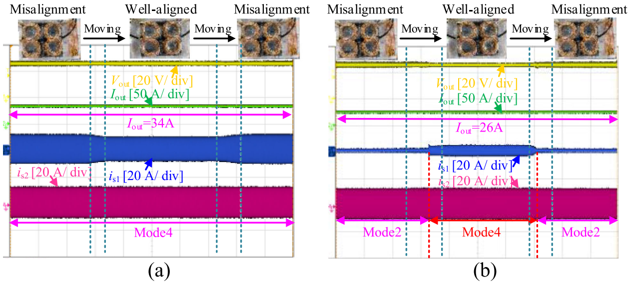

(a)

(b)

Fig. 26. Experimental dynamic response waveforms of $V_{\text{out}}$, $I_{\text{out}}$, $i_{s1}$, and $i_{s2}$ while the receiver is moving with (a) $I_{\text{out}} = 34$ A and (b) $I_{\text{out}} = 26$ A.

method is adopted, $I_{s1}$ and $I_{s2}$ are the same. While using the PPP control method, with the rectifiers operating in Mode 3, $I_{s2}$ is lower than $I_{s1}$. Thus, although the ZVS operation is achieved with both power distribution methods, the measured overall efficiency using the PPP method is up to 87.5%, which is improved by 1.3% compared with that of the conventional method.

Similarly, Fig. 18 contrasts $i_{t1}$, $i_{t2}$, $v_{\text{out1}}$, and $v_{\text{out2}}$ using two methods in light-load condition ($I_{\text{out}} \leq \lambda I_{t1}$) with $M_1 = M_2 = 8.7$ $\mu$H. The dc output voltage and current are maintained at 24 V and 18.5 A. Comparing the waveforms in Figs. 16(a) and 18(a), when using the conventional power distribution method, conducting angles in the light-load condition are smaller, resulting in more switching loss. The measured overall efficiency is sharply decreased from 86.2% to 72.1%. Fig. 18(b) shows the corresponding waveforms with the proposed PPP control method. In this case, only Receiver #2 is adjusted to regulate the system output current, while Receiver #1 is shut to avoid extra switching loss.

As shown in Fig. 19(a), when the conventional power distribution method is adopted, $I_{s1}$ and $I_{s2}$ are still the same. With the PPP control method, $I_{s1}$ is approximately equal to zero, which verifies the theoretical analysis. Besides, as shown in Fig. 19(b), the reactive component and harmonic content in $i_r$ with the PPP method are less than that with the conventional method, which reduces the turn-OFF loss of the inverter. The measured overall efficiency using the PPP method is up to 79.3%, which is improved by 7.2% compared with the conventional method.

*2) Waveforms of $M_{1\,1} < M_2$:* When $M_1 = 0.5{\cdot}M_2$ ($M_1 = {\sim}5$ $\mu$H and $M_2 = {\sim}10$ $\mu$H), the waveforms of the $i_{t1}$, $i_{t2}$, $v_{\text{out1}}$, and $v_{\text{out2}}$ using the conventional power distribution method are shown in Fig. 20(a). $V_{\text{out}}$ and $I_{\text{out}}$ are set as 24 V and 30 A. In this situation, rectifiers are still regulated with $\gamma_1 = \gamma_2$, while $I_{t1}$ is only half as $I_{t2}$, which results in high switching loss. Here, the measured system efficiency is 86.5%. While using the proposed PPP control method with Mode 4 under the same condition, only $\gamma_1$ is adjusted to suit the load requirements, and $\gamma_2$ is still fixed at $\pi$, as shown in Fig. 20(b). The measured overall efficiency is up to 89.6%, which is improved by 3.1% compared with the conventional method.

Moreover, with the PPP control method, the drain-source voltage and the gate-source voltage of the MOSFET $S_1$ in the rectifier and the MOSFET $P_1$ in the inverter are shown in Fig. 21. By setting the dead time of the active rectifier $\sigma_d = 300$ ns and the phase difference $\varphi_1 = \varphi_2 = 5°$, $v_{\text{gs\_}s1}$ and $v_{\text{gs\_}p1}$ always begin to turn to the high level after $v_{\text{ds\_}s1}$ and $v_{\text{ds\_}p1}$ are completely decreased to zero, which indicates that the ZVS operations are achieved in rectifiers and inverter.

### C. Efficiency Comparison and Analysis

Moreover, to offer a fair and complete comparison, a single-receiver WPT system with the *LCC–LCC* topology is also built. Here, the transmitter is remained, while only the receiver coil and its compensation network are replaced in the single-rectifier receiver. The key parameters of the single-receiver system are listed in Table IV. $L_{\text{sq}}$ is the self-inductance of the square receiver coil, while $C_{\text{sq}}$, $L_{\text{tq}}$, and $C_{\text{tq}}$ are the compensation elements in the *LCC* network. $R_{\text{sq}}$ and $R_{\text{tq}}$ are the ESRs in the corresponding loops. The receiver coil of the single receiver is shown in Fig. 22(a). To achieve the same maximum system output current, as shown in Fig. 22(b), the mutual inductance between the receiver coil and the transmitter coil $M_q$ is designed at 17.4 $\mu$H when the magnetic coupler is well-aligned. The receiver coil is designed with one-strand and seven-turns Litz wire and the same size as the BP receiver coils.

The trends of the overall system efficiency against the system output power with different misalignment distances are plotted in Fig. 23. When the magnetic coupler is well-aligned, the rectifiers will operate under Mode 2 and Mode 3 with the proposed

TABLE V
SUMMARY AND COMPARISON OF THE PREVIOUS LOW-VOLTAGE AND HIGH-CURRENT WPT SYSTEMS

| Reference | Power regulating method | Circuit structure | Compensation network | Output characteristic | Receiver coil size | Operating frequency | Coupling coefficient | Output power | Efficiency |
|---|---|---|---|---|---|---|---|---|---|
| [13] | DC-DC converter | Dual receiver | S-P | 30V-10A | 300mm*300mm*26mm | 10kHz | 0.35 | 300W | 88% |
| [14] |  | Singe receiver | S-S | 24V-75A | 220mm*220mm*10mm | 85kHz | 0.7 | 1.8kW | 89.9% |
| [18] |  | Singe receiver | LCC-LCC | 24V-75A | 220mm*220mm*10mm | 85kHz | 0.68~0.92 | 1.8kW | 88% |
| [19] | Half wave rectifier | Singe receiver | S-S | 48V-10A |  | 85kHz | 0.23 | 480W | 90.93% |
| This paper | Active Rectifier | Dual receiver | LCC-LCC | 24V-50A | 200mm*160mm*25mm | 200kHz | 0.35 | 1.2kW | 92.2% |

PPP control method, as shown in Fig. 23(a). Compared with the conventional power distribution method with the dual-receiver WPT system, the proposed method can improve the system efficiency by up to ∼9%. When the mutual inductances are unbalanced, the receiver will operate, respectively, under four modes at the corresponding load power demands with the PPP method. In this situation, the proposed method can increase the system efficiency by ∼10%, compared with the conventional method, as shown in Fig. 23(b) and (c). Meanwhile, the efficiency of the dual-receiver WPT system is always much higher than that of the single-receiver WPT system with the whole load range.

In Fig. 24, the power losses of each stage are analyzed under different mutual inductance conditions. Compared with the conventional power distribution method, when $M_1 = M_2$, the proposed PPP control method can decrease the rectifier loss by ∼26% @ $P_{\mathrm{out}} = 250$ W, ∼41% @ $P_{\mathrm{out}} = 500$ W, and ∼31% @ $P_{\mathrm{out}} = 750$ W. When $M_1 = 0.66{\cdot}M_2$, the rectifier loss can be reduced by ∼42% @ $P_{\mathrm{out}} = 250$ W, ∼26% @ $P_{\mathrm{out}} = 500$ W, and ∼24% @ $P_{\mathrm{out}} = 750$ W. Furthermore, the rectifier loss is reduced by ∼45% (@ $P_{\mathrm{out}} = 250$ W), ∼26% @ $P_{\mathrm{out}} = 500$ W, and by ∼24% @ $P_{\mathrm{out}} = 750$ W as $M_1 = 0.5{\cdot}M_2$. Besides, the inverter loss is also reduced with the proposed PPP control method, while the ESRs are maintained at a low level. In conclusion, with the PPP control method, the rectifier loss is reduced apparently in the experimental setup, which indicates the effectiveness for efficiency improvement of the proposed method.

### *D. Dynamic Response*

To verify the actual effect of the designed hysteresis control and PI control, the dynamic response waveforms of $V_{\mathrm{out}}$, $I_{\mathrm{out}}$, $i_{s1}$, and $i_{s2}$ when the load current is changing are provided in Fig. 25. With $M_1 = 0.5M_2$, when $I_{\mathrm{out}}$ varies slowly between 13 and 15 A, the receiver is switched between Mode 1 and Mode 3. During the load variation process in Fig. 25(a), $V_{\mathrm{out}}$ can be maintained at a constant value without noticeable oscillation or fluctuation, and no frequent switching phenomenon is observed. The same conclusion can also be obtained from Fig. 25(b) and (c), which show the dynamic response waveforms when $I_{\mathrm{out}}$ varies between 17 (Mode 3) and 20 A (Mode 2), and between 20 (Mode 2) and 26 A (Mode 4). Thus, the dynamic performance of the control system can be well proved.

Moreover, for the dynamic applications, the waveforms when the receiver moves with a low speed are shown in Fig. 26. While the receiver is moving, as shown in Fig. 26(a), $V_{\mathrm{out}}$ and $I_{\mathrm{out}}$ can be kept as 24 V and 34 A, and the receiver operates in Mode 4 stably. When $I_{\mathrm{out}}$ is set to 26 A, the designed hysteresis control will switch the receiver into the corresponding operating mode with different misalignment conditions, as shown in Fig. 26(b). Meanwhile, since the waveform of the rectifier input current is a smooth sine wave without visible harmonics and distortion, the sampling and the zero-crossing point detecting are relatively reliable and straightforward in the active rectifier with software phase-locked loop implemented in the DSP. Thus, in the experimental results, it is proved that the ZVS operation is well realized in a wide operating range, and no waveform distortion or considerable temperature rise caused by the hard-switching operating is observed. Furthermore, with the cooperation of the PI control and the hysteresis control, $V_{\mathrm{out}}$ and $I_{\mathrm{out}}$ can be maintained without noticeable overshoot or oscillation in the moving process, which indicates its good performance of dynamic response and stability.

### *E. Comparison With the Other Low-Voltage and High-Current Output WPT System for LEVs Charging*

In the last decades, several methods have been investigated for the low-voltage and high-current power supply system, e.g., LEVs charging application to achieve a high-power transfer efficiency [14], [15], [19], [20]. In [14], the dual-receiver system with a dc–dc converter is adopted, which results in low overall system efficiency. Besides, the volume of the receiver is also sacrificed due to the utilization of additional dc–dc converters. In [15], the series–series (S–S) compensation network is used in the 24 V–75 A output WPT system with ∼89.9% efficiency. However, the multistrands-paralleled Litz wire in the receiver coil increases the cost and the weight of the magnetic coupler. In [19], the *LCC–LCC* compensation network is employed in the low-voltage and high-current output WPT system with the optimized current stress of the receiver coil. However, with only one receiver, the power loss in the receiver cannot be further reduced. In [20], with the S–S topology and the dual half-wave rectifier, multiple loads can be supplied with a 10 A output current. Nevertheless, the receiver coil suffers from large current stress due to its single-receiver coil structure, lowering the overall efficiency.

Compared with the above literature, the main contribution of this article is to reduce the ESRs loss and optimize the switching loss in the dual-receiver WPT system by reallocating the power flow through the receivers. When the load required current varies, the proposed system can obtain a stable output with high overall efficiency. The comparisons are summarized and listed in Table V.

## V. CONCLUSION

In this article, an efficiency improving method based on the PPP control is proposed for the dual-receiver WPT system. According to the mathematical analysis of the switching loss on the active rectifiers, the operation modes of the receiver are divided into four categories, and the corresponding characteristics for four modes are summarized. To reduce the rectifier switching loss and improve the overall system efficiency, a closed-loop control strategy is designed for selecting the operation mode of the rectifiers and regulating their conducting angles. To verify the proposed method, a 24 V–50 A prototype is set up. The experimental results show that, compared with the conventional power distribution method based on the impedance matching, the proposed PPP method can improve the efficiency by 6%–7% with different misalignment situations, achieving as high as over 92.2% at the heavy load conditions.

## REFERENCES

[1] M. Fu, C. Ma, and X. Zhu, “A cascaded boost–buck converter for high-efficiency wireless power transfer systems,” *IEEE Trans. Ind. Informat.*, vol. 10, no. 3, pp. 1972–1980, Aug. 2014.

[2] J. Feng, Q. Li, F. Lee, and M. Fu, “Transmitter coils design for free-positioning omnidirectional wireless power transfer system,” *IEEE Trans. Ind. Informat.*, vol. 15, no. 8, pp. 4656–4664, Aug. 2019.

[3] J. Zhu, Y. Ban, Y. Zhang, Z. Yan, R. Xu, and C. Mi, “Three-coil wireless charging system for metal-cover smartphone applications,” *IEEE Trans. Power Electron.*, vol. 35, no. 5, pp. 4847–4858, May 2020.

[4] M. Huang, Y. Lu, and R. Martins, “A reconfigurable bidirectional wireless power transceiver for battery-to-battery wireless charging,” *IEEE Trans. Power Electron.*, vol. 34, no. 8, pp. 7745–7753, Aug. 2019.

[5] Y. Li *et al.*, “Analysis, design, and experimental verification of a mixed high-order compensations-based WPT system with constant current outputs for driving multi-string LEDs,” *IEEE Trans. Ind. Electron.*, vol. 67, no. 1, pp. 203–213, Jan. 2020.

[6] Z. Yan, Q. Siyao, Q. Zhu, L. Huang, and A. Hu, “A simple brightness and color control method for LED lighting based on wireless power transfer,” *IEEE Access*, vol. 6, pp. 51477–51483, 2018.

[7] D. Patil, M. McDonough, J. Miller, B. Fahimi, and P. Balsara, “Wireless power transfer for vehicular applications: Overview and challenges,” *IEEE Trans. Transp. Electrific.*, vol. 4, no. 1, pp. 3–37, Mar. 2018.

[8] A. Mohamed, A. Berzoy, and O. Mohammed, “Experimental validation of comprehensive steady-state analytical model of bidirectional WPT system in EVs applications,” *IEEE Trans. Veh. Technol.*, vol. 66, no. 7, pp. 5584–5594, Jul. 2017.

[9] L. Zhao, D. Thrimawithana, and U. Madawala, “Hybrid bidirectional wireless EV charging system tolerant to pad misalignment,” *IEEE Trans. Ind. Electron.*, vol. 64, no. 9, pp. 7079–7086, Sep. 2017.

[10] A. Babaki, S. Vaez-Zadeh, A. Zakerian, and G. Covic, “Variable-frequency retuned WPT system for power transfer and efficiency improvement in dynamic EV charging with fixed voltage characteristic,” *IEEE Trans. Energy Convers.*, vol. 36, no. 3, pp. 2141–2151, Sep. 2021.

[11] W. Zhang, J. White, A. Abraham, and C. Mi, “Loosely coupled transformer structure and interoperability study for EV wireless charging systems,” *IEEE Trans. Power Electron.*, vol. 30, no. 11, pp. 6356–6367, Nov. 2015.

[12] Y. Li, W. Sun, X. Zhu, and J. Hu, “A hybrid modulation control for wireless power transfer systems to improve efficiency under light-load conditions,” *IEEE Trans. Ind. Electron.*, to be published, doi: 10.1109/TIE.2021.3102411.

[13] Y. Li *et al.*, “A new coil structure and its optimization design with constant output voltage and constant output current for electric vehicle dynamic wireless charging,” *IEEE Trans. Ind. Informat.*, vol. 15, no. 9, pp. 5244–5256, Sep. 2019.

[14] A. Zaheer, G. Covic, and D. Kacprzak, “A bipolar pad in a 10-kHz 300-W distributed IPT system for AGV applications,” *IEEE Trans. Ind. Electron.*, vol. 61, no. 7, pp. 3288–3301, Jul. 2014.

[15] F. Lu *et al.*, “A low-voltage and high-current inductive power transfer system with low harmonics for automatic guided vehicles,” *IEEE Trans. Veh. Technol.*, vol. 68, no. 4, pp. 3351–3360, Apr. 2019.

[16] Z. Zhang and B. Zhang, “Omnidirectional and efficient wireless power transfer system for logistic robots,” *IEEE Access*, vol. 8, pp. 13683–13693, 2020.

[17] X. Dai, J. Wu, J. Jiang, R. Gao, and U. Madawala, “An energy injection method to improve power transfer capability of bidirectional WPT system with multiple pickups,” *IEEE Trans. Power Electron.*, vol. 36, no. 5, pp. 5095–5107, May 2021.

[18] H. He *et al.*, “Maximum efficiency tracking for dynamic WPT system based on optimal input voltage matching,” *IEEE Access*, vol. 8, pp. 215224–215234, 2020.

[19] F. Lu *et al.*, “A tightly coupled inductive power transfer system for low-voltage and high-current charging of automatic guided vehicles,” *IEEE Trans. Ind. Electron.*, vol. 66, no. 9, pp. 6867–6875, Sep. 2019.

[20] C. Zhu *et al.*, “Analysis and design of cost-effective WPT systems with dual independently regulatable outputs for automatic guided vehicles,” *IEEE Trans. Power Electron.*, vol. 36, no. 6, pp. 6183–6187, Jun. 2021.

[21] Y. Li, T. Lin, R. Mai, L. Huang, and Z. He, “Compact double-sided decoupled coils-based WPT systems for high-power applications: Analysis, design, and experimental verification,” *IEEE Trans. Transp. Electrific.*, vol. 4, no. 1, pp. 64–75, Mar. 2018.

[22] S. Zhou and C. Mi, “Multi-paralleled LCC reactive power compensation networks and their tuning method for electric vehicle dynamic wireless charging,” *IEEE Trans. Ind. Electron.*, vol. 63, no. 10, pp. 6546–6556, Oct. 2016.

[23] U. Schwalbe, M. Schilling, B. Koehnlechner, and T. Reimann, “Challenges in low-voltage high-current applications—Fathom the limits in system design,” in *Proc. Int. Conf. Integr. Power Electron.*, 2016, pp. 1–7.

[24] B. Zhao, Q. Song, W. Liu, and Y. Sun, “Overview of dual-active-bridge isolated bidirectional DC-DC converter for high-frequency-link power-conversion system,” *IEEE Trans. Power Electron.*, vol. 29, no. 8, pp. 4091–4106, Aug. 2014.

[25] S. Inoue and H. Akagi, “A bidirectional isolated DC-DC converter as a core circuit of the next-generation medium-voltage power conversion system,” *IEEE Trans. Power Electron.*, vol. 22, no. 2, pp. 535–542, Mar. 2007.

[26] Z. Yan *et al.*, “Efficiency improvement of wireless power transfer based on multi-transmitter system,” *IEEE Trans. Power Electron.*, vol. 35, no. 9, pp. 9011–9023, Sep. 2020.

[27] G. Ning, S. Wang, G. Zheng, Y. Liu, and M. Fu, “A novel passive current sharing method for a two-transmitter one-receiver WPT system,” in *Proc. IEEE 9th Int. Power Electron. Motion Control Conf.*, 2020, pp. 985–990.

[28] M. Fu, H. Yin, M. Liu, Y. Wang, and C. Ma, “A 6.78 MHz multiple-receiver wireless power transfer system with constant output voltage and optimum efficiency,” *IEEE Trans. Power Electron.*, vol. 33, no. 6, pp. 5330–5340, Jun. 2018.

[29] M. Fu, T. Zhang, C. Ma, and X. Zhu, “Efficiency and optimal loads analysis for multiple-receiver wireless power transfer systems,” *IEEE Trans. Microw. Theory Techn.*, vol. 63, no. 3, pp. 801–812, Mar. 2015.

[30] D. Pehrman, Y. Liu, C. Cui, and X. Huang, “Loss reduction by synchronous rectification in a 50 kW sic-based inductive power transfer system,” in *Proc. 46th Annu. Conf. IEEE Ind. Electron. Soc.*, 2020, pp. 3907–3912.

[31] R. Bosshard and J. Kolar, “All-SiC 9.5 kW/dm$^3$ on-board power electronics for 50 kW/85 kHz automotive IPT system,” *IEEE J. Emerg. Sel. Topics Power Electron.*, vol. 5, no. 1, pp. 419–431, Mar. 2017.

[32] A. Q. Cai and L. Siek, “A 2-kW, 95% efficiency inductive power transfer system using gallium nitride gate injection transistors,” *IEEE J. Emerg. Sel. Topics Power Electron.*, vol. 5, no. 1, pp. 458–468, Mar. 2017.

[33] T. Mishima and E. Morita, “High-frequency bridgeless rectifier based ZVS multi-resonant converter for inductive power transfer featuring high-voltage GaN-HFET,” *IEEE Trans. Ind. Electron.*, vol. 64, no. 11, pp. 9155–9164, Nov. 2017.

[34] T. Mishima and E. Morita, “Comparative evaluation of secondary-side ZVS-PWM controlled GaN-HFET resonant converters for inductive power transfer,” in *Proc. IEEE Energy Convers. Congr. Expo.*, 2017, pp. 2610–2617.

[35] Y. Li *et al.*, “Extension of ZVS region of series–series WPT systems by an auxiliary variable inductor for improving efficiency,” *IEEE Trans. Power Electron.*, vol. 36, no. 7, pp. 7513–7525, Jul. 2021.

[36] Y. Jiang, L. Wang, J. Fang, R. Li, R. Han, and Y. Wang, “A high-efficiency ZVS wireless power transfer system for electric vehicle charging with variable angle phase shift control,” *IEEE J. Emerg. Sel. Topics Power Electron.*, vol. 9, no. 2, pp. 2356–2372, Apr. 2021.

[37] Y. Jiang, L. Wang, J. Fang, C. Zhao, K. Wang, and Y. Wang, "A joint control with variable ZVS angles for dynamic efficiency optimization in wireless power transfer system," *IEEE Trans. Power Electron.*, vol. 35, no. 10, pp. 11064–11081, Oct. 2020.

[38] D. Christen and J. Biela, "Analytical switching loss modeling based on datasheet parameters for MOSFETs in a half-bridge," *IEEE Trans. Power Electron.*, vol. 34, no. 4, pp. 3700–3710, Apr. 2019.

[39] D. Neumayr, M. Vöhringer, N. Chrysogelos, G. Deboy, and J. Kolar, "p$^3$DCT—Partial-power pre-regulated DC transformer," *IEEE Trans. Power Electron.*, vol. 34, no. 7, pp. 6036–6047, Jul. 2019.

[40] J. Zientarski, M. Martins, J. Pinheiro, and H. Hey, "Evaluation of power processing in series-connected partial-power converters," *IEEE J. Emerg. Sel. Topics Power Electron.*, vol. 7, no. 1, pp. 343–352, Mar. 2019.

[41] V. Iyer, S. Gulur, G. Gohil, and S. Bhattacharya, "An approach towards extreme fast charging station power delivery for electric vehicles with partial power processing," *IEEE Trans. Ind. Electron.*, vol. 67, no. 10, pp. 8076–8087, Oct. 2020.

[42] J. Anzola, I. Aizpuru, A. Arruti, A. Alacano, and C. Bernal, "Review of architectures based on partial power processing for DC-DC applications," *IEEE Access*, vol. 8, pp. 103405–103418, 2020.

[43] N. Bac, D. Vilathgamuwa, and U. Madawala, "A sic-based matrix-converter topology for inductive power transfer system," *IEEE Trans. Power Electron.*, vol. 29, no. 8, pp. 4029–4038, Aug. 2014.

[44] H. Raee, A. Rabiei, and T. Thirnger, "Analytical prediction of switching losses in MOSFETs for variable drain-source voltage and current applications," in *Proc. IEEE 8th Conf. Ind. Electron. Appl.*, 2013, pp. 705–709.

[45] W. Eberle, Z. Zhang, Y. Liu, and P. Sen, "A practical switching loss model for buck voltage regulators," *IEEE Trans. Power Electron.*, vol. 24, no. 3, pp. 700–713, Mar. 2009.

[46] F. Lu, H. Zhang, H. Hofmann, W. Su, and C. Mi, "A dual-coupled LCC compensated IPT system with a compact magnetic coupler," *IEEE Trans. Power Electron.*, vol. 33, no. 7, pp. 6391–6402, Jul. 2018.

[47] H. Zhang, C. Zhu, and F. Lu, "A compact and low-distortion inductive charging system for automatic guided vehicles based on LCC compensation and integrated magnetic coupler," in *Proc. IEEE Transp. Electrific. Conf. Expo.*, 2019, pp. 1–5.

[48] P. Zhang, M. Saeedifard, O. Onar, Q. Yang, and C. Cai, "A field enhancement integration design featuring misalignment tolerance for wireless EV charging using LCL topology," *IEEE Trans. Power Electron.*, vol. 36, no. 4, pp. 3852–3867, Apr. 2021.

**Shunpan Liu** (Student Member, IEEE) received the B.S. degree in electrical engineering and automation from the School of Electrical Engineering, Southwest Jiaotong University, Chengdu, China, in 2018, where he is currently working toward the Ph.D. degree.

His research interests include wireless power transfer, especially on control method and circuit topology of dynamic inductive power transfer system.

**Xing Zhao** (Member, IEEE) received the B.Eng. degree from the Nanjing University of Aeronautics and Astronautics, Nanjing, China, in 2014, and the Ph.D. degree from The Hong Kong Polytechnic University, Hong Kong, in 2020, both in electrical engineering.

From July 2019 to January 2020, he was a Visiting Research Scholar with the Center for Advanced Power Systems, Florida State University, Tallahassee, FL, USA. Between July 2020 and October 2021, he served as a Research Assistant Professor with the Department of Electrical Engineering, The Hong Kong Polytechnic University. Since November 2021, he has been a Lecturer with the School of Physics, Engineering and Technology, University of York, York, U.K. He has authored or coauthored more than 50 technical papers in the international journals and conferences and holds 6 granted patents. His research interests include advanced electrical machines and power electronics for electric vehicles and renewable energy systems.

**Yihao Wu** (Student Member, IEEE) received the B.Eng. degree in electronic and electrical engineering from Southwest Jiaotong University, Chengdu, China, the B.Eng. (first class hons.) degree from the University of Leeds, Leeds, U.K., both in 2020, and the M.Sc. (distinction) degree in control systems from Imperial College London, London, U.K., in 2021. He is currently working toward the Ph.D. degree in electrical engineering with the Department of Engineering, University of Cambridge, Cambridge, U.K.

His research interests include wireless power transfer.

**Lingyun Zhou** (Student Member, IEEE) received the B.S. degree in electrical engineering and automation in 2018 from the School of Electrical Engineering, Southwest Jiaotong University, Chengdu, China, where she is currently working toward the Ph.D. degree.

Her research interests include wireless power transfer, especially on efficiency improvement for low-power devices.

**Yong Li** (Senior Member, IEEE) received the B.Sc. and Ph.D. degrees from the School of Electrical Engineering, Southwest Jiaotong University, Chengdu, China, in 2013 and 2017, respectively.

From 2017 to 2018, he was a Research Associate with the Department of Electrical Engineering, The Hong Kong Polytechnic University, Hong Kong, and subsequently, he was a Postdoctoral Fellow. He is currently an Associate Professor with Southwest Jiaotong University. His research interests include wireless power transfer and microgrids.

Dr. Li is a Guest Editor of Electronics for a special issue Wireless Power Transfer and Its Applications.

**Ruikun Mai** (Senior Member, IEEE) received the B.Sc. and Ph.D. degrees in electrical engineering from the School of Electrical Engineering, Southwest Jiaotong University, Chengdu, China, in 2004 and 2010, respectively.

He is currently a Professor with the School of Electrical Engineering, Southwest Jiaotong University, Chengdu, China. His research interests include wireless power transfer and its application in railway systems, power system stability and control.

**Zhengyou He** (Senior Member, IEEE) received the B.S. and M.S. degrees from Chongqing University, Chongqing, China, in 1992 and 1995, respectively, and the Ph.D. degree from Southwest Jiaotong University, Chengdu, China, in 2001.

Since 2002, he has been a Professor with the School of Electrical Engineering, Southwest Jiaotong University. He was a Visiting Scholar with Cornell University, New York, NY, USA, from 2008 to 2009. His research interests include area of signal processing and information theory and its application in electrical power systems, and the application of wavelet transforms in power systems.